

EXPERIMENTAL AND FINITE ELEMENT ANALYSIS OF ASYMMETRIC ROLLING OF 6061 ALUMINUM ALLOY USING TWO-SCALE ELASTO-PLASTIC CONSTITUTIVE RELATION

The goal of this work was theoretical and experimental study of micro- and macroscopic mechanical fields of 6061 aluminum alloy induced by the asymmetric rolling process. Two-scale constitutive law was used by implementing an elasto-plastic self-consistent scheme into the Finite Element code (ABAQUS/Explicit). The model was applied to study the asymmetric rolling. Such a deformation process induces heterogeneous mechanical fields that were reproduced by the model thanks to the crystallographic nature of constitutive law used. The studied material was processed, at room temperature, in one rolling pass to 36% reduction. The resulting material modifications were compared with predictions of the two-scale model. Namely, the calculated textures were compared with experimental ones determined by X-ray diffraction. Especially, detailed quantitative analysis of texture variation across the sample thickness was done. The influence of this texture variation on plastic anisotropy was studied. The advantages of asymmetric rolling process over symmetric one were identified. The main benefits are a nearly homogeneous crystallographic texture, reduced rolling normal forces and homogenization of plastic anisotropy through the sample thickness.

Keywords: asymmetric rolling; 6061 aluminum; finite element method; crystalline deformation model; texture

1. Introduction

Asymmetric rolling (AR) offers numerous possibilities of material properties modification and of the improvement of technological process parameters. AR process can be achieved by modification of rolling mills, commonly used for symmetric rolling (SR). This type of rolling can optimize industrial applications because it reduces the applied rolling forces, changes the shape of rolled plate and modifies the material microstructure (e.g., [1-5]). During AR process a strong shear stress is induced in a material, which produces an important shear strain and, consequently, modifies resulting crystallographic textures. It was observed that the shear deformation texture, containing the $\{111\}$ //ND fiber (where ND is normal direction), improves the formability and strength of aluminum alloy sheets [5]. Moreover, AR can be used to refine considerably a material microstructure (e.g., [6-8]). There is a rich literature on asymmetric rolling of materials with different crystal structures (e.g., [9-19]), among them numerous are those devoted to aluminum [15-19]. However, most of them are focused on rolling processes in multiple passes up to high thickness reduction. When one simulates AR processes with multiple passes using Finite Element Method (FEM), an additional constraint has to be added in order to avoid the occurrence of sheet bending at the end of

each pass [5,19]. Therefore, the effect of sample bending cannot be studied in such the approach and a real shape of material is not correctly predicted. Furthermore, most experimental and numerical studies, conducted on AR and available in the literature, were performed for thick sheets (e.g., [18,20]) while in many practical applications the rolling process starts from initially thin sheets.

In this work, the modifications of crystallographic texture and of mechanical characteristics, caused by the AR of aluminum samples, were studied using a finite element (FE) software with implemented polycrystalline deformation model (see e.g., [21]). The case of rolling in one pass (up to 36% reduction) of the initially thin samples is discussed in this paper. This is a typical reduction value, which can be attained in AR process without slipping occurrence between rolls and material. Calculated textures and stress-strain curves were compared with corresponding experimental results. It should be emphasized that crystallographic texture is a very sensitive issue of a deformation process. Therefore, texture modifications and its variation across the sample thickness were examined. The predicted texture variations were compared with experimental ones. It is well recognized that the crystallographic texture influences various material properties. One of them is plastic anisotropy, which is analyzed in the last section of the paper.

* AGH UNIVERSITY OF SCIENCE AND TECHNOLOGY, FACULTY OF PHYSICS AND APPLIED COMPUTER SCIENCE, AL. MICKIEWICZA 30, 30-059 KRAKÓW, POLAND

** LSPM-CNRS, UNIVERSITÉ PARIS 13, 99, AV. J.B. CLÉMENT, 93 430 VILLETANEUSE, FRANCE

*** UNIVERSITY OF LORRAINE – ENIM, LABPS, 1, ROUTE D'ARS LAQUENEXY CS 65820, 57078 METZ CEDEX 3, FRANCE

[#] Corresponding author: wierzbanowski@fis.agh.edu.pl

2. Implementation of crystallographic model into Finite Element software

Non-uniformity of stress and strain fields, which appears during AR and SR, can be examined by implementation of a crystallographic constitutive model into finite element (FE) code. In this work a simplified version of the self-consistent scheme of polycrystalline elasto-plastic deformation model, developed by Hill [22], was used. It is based on the works developed by Leffers [23] and Berveiller [24] and further strongly developed by Wierzbowski et al. [25-27], which is called LW model in this study. The elasto-plastic isotropic interaction between a grain and a surrounding material is expressed as:

$$\dot{\sigma}_{ij} = \sum_{ij} \dot{\epsilon}_{ij} + L \left(\dot{E}_{ij}^p - \dot{\epsilon}_{ij}^p \right) \quad (1)$$

where $\dot{\sigma}_{ij}$ and $\dot{\epsilon}_{ij}^p$ are the components of the stress and plastic strain rate tensors of a grain, \sum_{ij} are the components of the stress rate tensor applied to the sample, \dot{E}_{ij}^p are the global plastic strain rate tensor components and L states for an interaction parameter. Eq. (1) is a simplified version of the relation derived by Hill [22], in which the plastic strain substituted the total strain and the forth-rank interaction tensor was replaced by the L parameter. To ensure experimentally observed soft interactions between grains and the surrounding materials the scalar interaction parameter L has to be a fraction α of the elastic shear modulus G , i.e. $L = \alpha G$. α is called elasto-plastic interaction coefficient, which takes values of the order of 0.01 [23,24, 28]. Consequently, for the case of the aluminum alloy studied here, $L = 200$ MPa was chosen. Let us recall some basic elements of the crystalline model necessary for the understanding of the ongoing discussion.

A slip system s is defined by two unit vectors \mathbf{m}^s and \mathbf{n}^s respectively parallel to the slip direction $[uvw]$ and the slip plane normal (hkl) . Such a system becomes active if the resolved shear stress $\tau^s = \sigma_{[uvw](hkl)} = m_i^s \sigma_{ij} n_j^s$ on this system reaches a critical value τ_{cr}^s (the Schmid law), i.e. $\tau^s = \tau_{cr}^s$. During the deformation process, τ_{cr}^s increases due to the work hardening. This phenomenon is described by the following hardening rule:

$$\dot{\tau}_{cr}^s = \sum_r H^{sr} \left(\tau_{cr}^s \right) \dot{\gamma}^r \quad (2)$$

where $\dot{\tau}_{cr}^s$ is the rate of critical shear stress and $\dot{\gamma}^r$ is the plastic slip rate on s^{th} and r^{th} slip systems, respectively. The hardening matrix $[H]$ defines the rate of this increase. Its components obey a nonlinear law:

$$H^{sr} = h_o \left(1 - \frac{\tau_{cr}^s}{\tau_{sat}} \right)^a q^{sr} \quad (3)$$

expressing the saturation hardening phenomenon. τ_{sat} is the saturation value of the critical shear stress. Similarly as the initial critical shear stress, $\tau_o = \tau_{cr}^s|_{\dot{\gamma}^s=0}$, it has the same value for all systems belonging to a given slip system family. h_o specifies the hardening magnitude and a is a constant (cf. [28]). The term q^{sr} describes interactions among dislocations on the active slip systems. Its structure, in the simplest approach adopted here,

reflects the difference between the self-hardening (diagonal terms) and the latent hardening:

$$q^{sr} = \begin{cases} 1 & \text{if } s = r \\ d & \text{otherwise} \end{cases} \quad (4)$$

In the above definition $d > 1$ concerns strongly interacting slip systems, while the self-hardening corresponds to the weak one. Obviously, isotropic hardening occurs if $d = 1$. The parameters of hardening law can be partly identified from the tensile stress-strain curves.

For a given loading increment and each grain in turn, the most loaded active slip system s is identified and a small elementary plastic slip $\delta\gamma$ is performed leading to the elementary increments of the plastic strain:

$$\delta\epsilon_{ij}^p = \frac{1}{2} \left(m_i^s n_j^s + m_j^s n_i^s \right) \delta\gamma \quad (5)$$

and the lattice rotation:

$$\delta\omega_{ij}^{lat} = -\frac{1}{2} \left(m_i^s n_j^s - m_j^s n_i^s \right) \delta\gamma \quad (6)$$

The action is repeated, cumulating the plastic strains and lattice rotations, until all slip systems of the considered grain aggregate cease to be active in a given loading increment.

As it was already mentioned, to study the deformation process of complex structures the FE method is usually applied, e.g. [5,10, 29-31]. In the present work FE calculations were done using ABAQUS/Explicit software [32]. The crystallographic model was implemented into ABAQUS via the user subroutine VUMAT. A representative polycrystalline model samples were associated with each Gauss point of every finite element. Calculations in ABAQUS software are carried out incrementally following the principle illustrated in Fig. 1.

First, at the beginning of a loading increment, the ABAQUS program transfers to the VUMAT procedure an increment of the assumed total strain ΔE_{ij} to be attained as well as the stress and strain states obtained at the end of the preceding increment. The crystallographic model performs the imposed deformation ΔE_{ij} and calculates a new resulting stress state, which is transferred to ABAQUS. All state variables, such as elastic and plastic strains, plastic slips, crystallographic orientations and hardening data are also updated in the VUMAT routine.

3. Experimental procedure

6061 Aluminum alloy, with 2.4% Mg, was selected for the analysis as it is commonly used, for instance in automotive industry. The microstructure of this material was studied in [33,34]. The initial size of the samples was $60 \times 30 \times 2.9$ mm³. Rolling was performed in one pass till the thickness reduction of 36%. The diameter of both rolls was $R = 180$ mm. The asymmetry of the rolling process was obtained thanks to different angular velocities of the top and bottom rolls, ω_1 and ω_2 respectively, driven by independent motors (Fig. 2). The

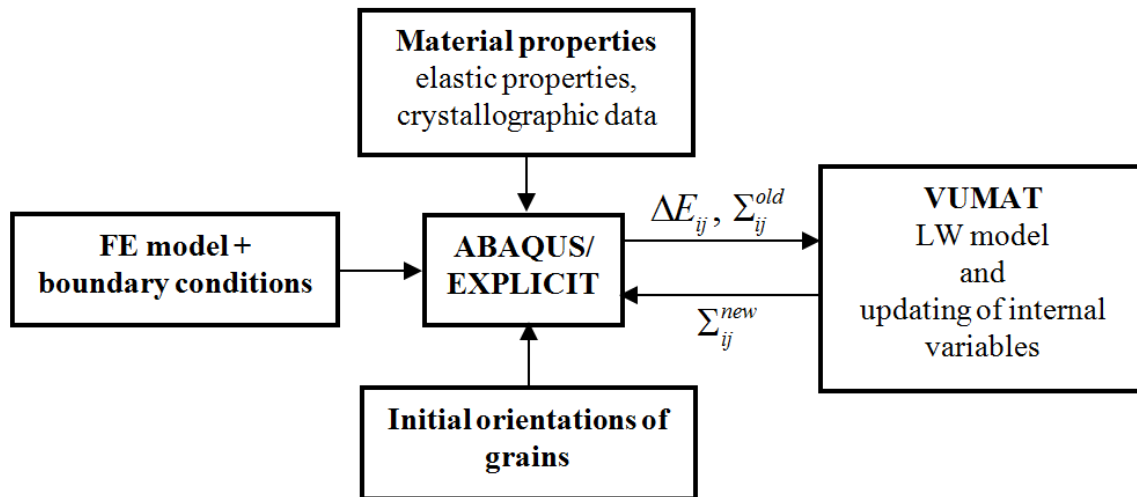


Fig. 1. Interaction of LW model, encrypted in VUMAT subroutine, with ABAQUS program

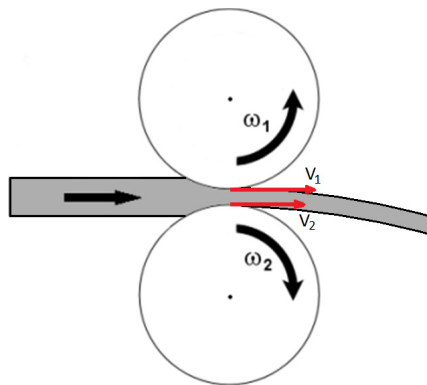


Fig. 2. Scheme of the studied asymmetric rolling process: two identical rolls turn with different angular velocities and $v_1 = \omega_1 R$, $v_2 = \omega_2 R$, where R is the radius of rollers

degree of asymmetry of the process can thus be quantified by the parameter A such that:

$$A = \frac{\omega_1}{\omega_2} \quad (7)$$

In the reported experiments, the angular velocity of the bottom roll was kept constant at 10 rpm and that of the top roll was imposed in order to obtain required values of the asymmetry ratio A ranging between 1.0 and 2.0. No lubrication was applied to the rolls, but the surfaces of rolls were rubbed with a silicon carbide paper along the rolling direction in order to increase the friction between the sample and the rolls. The crystallographic texture and microstructure were examined in two near-surface layers of the thickness about 20 μm (i.e. top and bottom surface layers) and also in the center layer of the rolled bar. Before examination the samples were mechanically polished with silicon carbide paper down to grade 4000 and then electro-polished in the solution A2 provided by Struers. The evolution of the crystallographic texture in the deformed samples was examined using X-ray diffraction. The $\{200\}$, $\{111\}$ and $\{220\}$ pole figures were measured and next the orientation distribution functions [35,36] were calculated.

4. Finite Element model

4.1. Mesh and boundary and initial conditions

The three-dimensional FE models of rolled samples were built using 8-node tri-linear brick elements. The model was built in such a way that the rolling direction (RD) and transversal direction (TD) coincided with X1 and X2 axes, respectively. Reduced integration technology was used with one integration point located in the element center. It was assumed in ABAQUS calculations that the sample did not deform along TD (i.e. $E_{22} = 0$ – usual approximation for rolling). Consequently, the mesh contained only one element through the transversal direction with the nodes constrained in X2 direction ($U_2 = 0.0$). The FE model totaled 128 finite elements: 16 along rolling and 8 along normal direction. The initial model size was the same as that of the experimental samples. The considered rolling reduction was 36% corresponding to the final sample thickness of 1.86 mm. The calculations were done for the same values of the asymmetry ratios as those used during the experimental tests. The friction coefficient of $\mu = 0.30$ was estimated on the basis of the capture angle [37]. The rolls were modeled as rigid bodies, using the *RIGID SURFACE option in ABAQUS software.

Polycrystalline samples represented by 150 grains were attached to each of 128 finite elements of the C3D8R type, which gives a total number of 19200 grains. Initial crystallographic orientations of grains were deduced from the initial texture of aluminum samples, measured by X-ray diffraction and shown in Fig. 3.

4.2. Identification of material properties

The mechanical properties of the model were adjusted by fitting the experimental tensile stress-strain curves. The case of tensile test along X1 direction was considered. Fig. 4 shows the FE mesh constituted by one 8-node brick element. The deformed mesh as well as the elasto-plastic behavior were assigned to

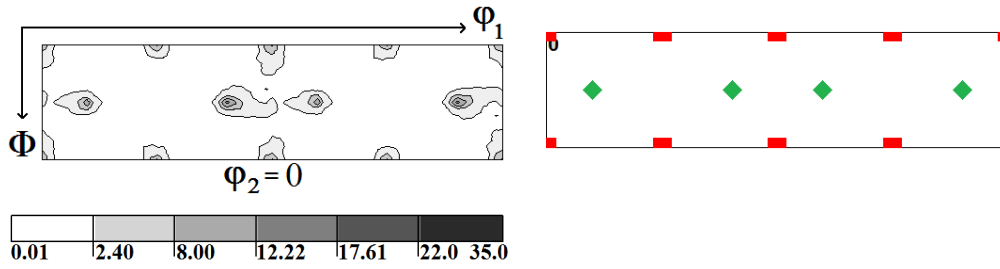


Fig. 3. Crystallographic texture of the initial aluminum samples determined by X-ray diffraction. $\varphi_2 = 0^\circ$ section is shown (Φ varies in the $[0, 90^\circ]$ range and φ_1 in the $[0, 360^\circ]$ range). Two ideal orientations of f.c.c rolling texture are marked: ■ – cubic orientation (W) and ◆ – Brass orientation (B)

this element. 150 grains with the orientation distribution close to the initial experimental texture were attached to each Gauss point. Isotropic ($d = 1$) and non-linear hardening was used in LW model, see Eqs. 3 and 4. The parameters τ_0 , h_o , τ_{sat} and a were determined by adjustment of the predicted stress-strain curves to

the experimental ones. An obtained perfect fit is shown in Fig. 5. The determined parameters and other mechanical constants characterizing aluminum samples are listed in Table 1.

4.3. Verification of quasi static rolling conditions

The VUMAT subroutine is dedicated to treat the dynamic problems using explicit integration algorithm. Typical time increments are of the order of 10^{-6} s in the case of mesh size of about 5 mm and the longitudinal wave celerity is of the order of 5000 m/s. So, this algorithm is well adapted to treat rapid dynamic problems such as crash simulation. In the case of the studied rolling process the number of time increments becomes excessively large. In order to reduce the calculation time the deformation rate was increased and the mass-scaling factor equal to 5 was applied to reduce the wave celerity. Mass-scaling factor changes artificially density of the material, which in turn changes the time step size. This method is commonly used for reducing run times in quasi-static analysis.

Time scaling factor was not used in the simulations. However, in such the situation, the inertial forces may become exaggerated and a question arises, whether one still deals with a quasi-static process. In order to verify this condition the kinetic energy was controlled during calculations. For a quasi-static process the kinetic energy of the deformed material should not exceed a small fraction of the internal energy [32]. An example of the variation of both types of energy vs. calculation time is shown in Fig. 6 in the case of symmetric rolling. The obtained result confirms that the criterion for a quasi-static process is fairly fulfilled.

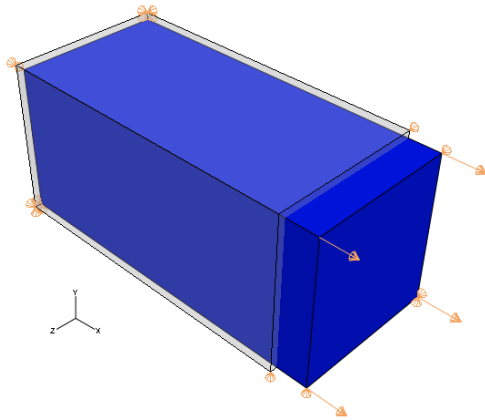


Fig. 4. FE model of tensile test along X1 direction. One element of C3D8R type with 8-nodes was used and 150 grains, reproducing initial crystallo-graphic texture of the sample, were attributed to this element

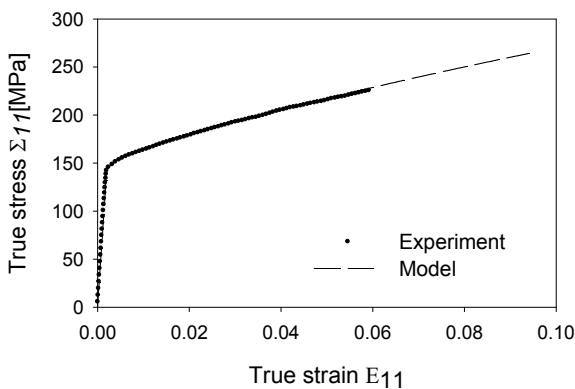


Fig. 5. Comparison of the experimental and calculated (FEM+LW model) tensile stress-strain curves for polycrystalline aluminum sample

TABLE 1

Material parameters for 6061 aluminum alloy. The hardening parameters were found by fitting the calculated stress-strain curves to the experimental ones

E [GPa]	ν	π [kg/m ³]	Slip systems	τ_0 [MPa]	h_o [MPa]	d	τ_{sat} [MPa]	a
70	0.34	2700	{111}<110>	70	390	1	235	1.2

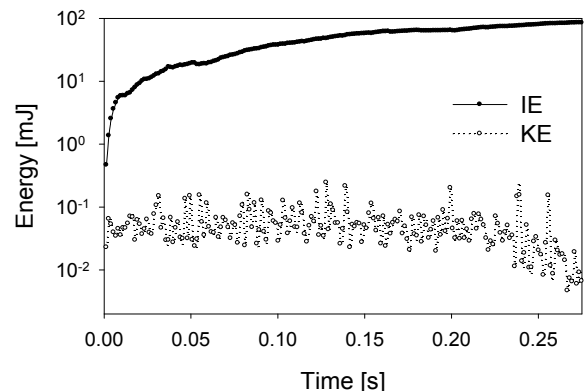


Fig. 6. Kinetic and internal energies (KE and IE) versus total simulation time for symmetric rolling of polycrystalline aluminum ($A = 1.0$)

5. Mechanical characteristics of asymmetrically rolled aluminum

The stress distribution during deformation process is of basic importance for resulting material properties. The stress and strain states result in our FEM calculations from the imposed geometry of the rolling process, i.e., by radii of rolls, their velocities and friction coefficient. There is no slippage between rolls and the material. The comparison of the global Σ_{13} and Σ_{33} stress fields during rolling is presented in Fig. 7. The images correspond to three values of asymmetry ratio, namely $A = 1.0$ (SR), $A = 1.05$ (weakly AR) and $A = 1.3$ (AR). One can observe that during SR the shear stresses component Σ_{13} has the opposite sequence of signs on top and bottom surface layers (Fig. 7a – left column). In contrast, when the rolling asymmetry increases, i.e., for $A = 1.3$, there is no change of sign and the distribution of the Σ_{13} shear stress component becomes nearly homogeneous across the sample thickness (Fig. 7c – left column). This result is in qualitative agreement with FEM calculations for isotropic material [10].

The distribution of the Σ_{33} component of the global stress for SR and AR is shown in Fig. 7 – right column. It is nearly homogeneous across the sample thickness and its magnitude decreases vs. rolling asymmetry, i.e., it is lower for AR ($A = 1.3$ and $A = 1.05$) than for SR ($A = 1.0$). These facts (homogeneity and lower magnitude) explain the presence of lower residual stresses

in asymmetrically rolled material sheets [14], as determined by diffraction measurements (for such type of measurements see e.g. [38,39]).

Also, the external actions of the rolling process were examined. One of the advantages of AR, predicted as well by FEM calculations, is the reduction of the average normal force (F_{AR}) exerted on the sample surfaces. This is a consequence of a reduction of the magnitude of the normal component of the global stress Σ_{33} , representing the normal compression of the material by rolls (cf., Fig. 7-right column). The predicted normal force (presented as the relative value F_{AR}/F_{SR}) versus A is shown in Fig. 8a. A strong reduction (of nearly 30% for $A > 1.3$) of this force with increasing of rolling asymmetry is obtained. Also the sample curvature versus A was calculated and is shown in Fig. 8b. This curvature is defined by the deflection of the end section of the rolled sheet. As expected, no bending was predicted for symmetric rolling, $A = 1.0$. Also, it is visible that the sign of the curvature radius changes between $A = 1.1$ and $A = 1.3$. This means that for A equal approximately 1.2 the sheet deflection is also nil. This result was confirmed experimentally in the case of asymmetrically rolled technically pure copper – Fig. 9 (copper has the same crystal structure and deformation mechanisms as aluminum). In the presented experimental results one observes the change of curvature sign between $A = 1.1$ and $A = 1.25$ (Fig. 9). Moreover, it can be seen in Fig. 8 that the sample cur-

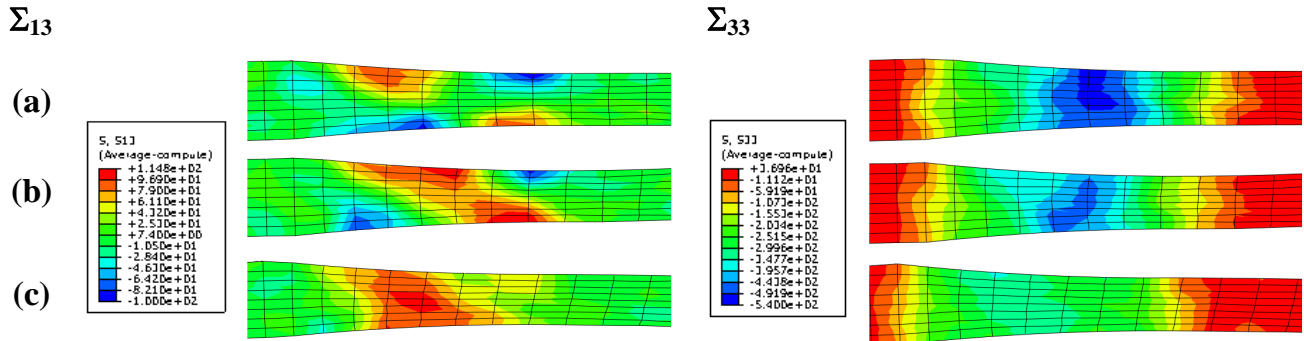


Fig. 7. Calculated distributions of Σ_{13} and Σ_{33} global stress components during rolling with asymmetry ratios $A = \omega_1/\omega_2$ equal to: (a) 1, (b) 1.05 and (c) 1.3. Calculations were done for polycrystalline aluminum rolled to 36% reduction in one pass (FEM+LW model)

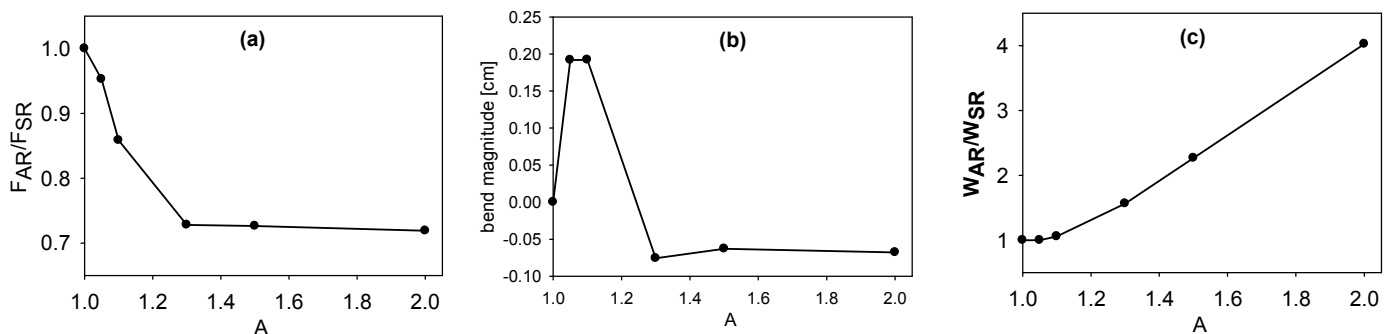


Fig. 8. Mechanical characteristics versus $A = \omega_1/\omega_2$ predicted by FEM+LW model for polycrystalline aluminum (rolled to 36% reduction in one pass): a) relative normal force (F_{AR}/F_{SR}), b) sample curvature defined as a deflection (in cm) at the end of 20 cm rolled plate, c) relative deformation work (W_{AR}/W_{SR})

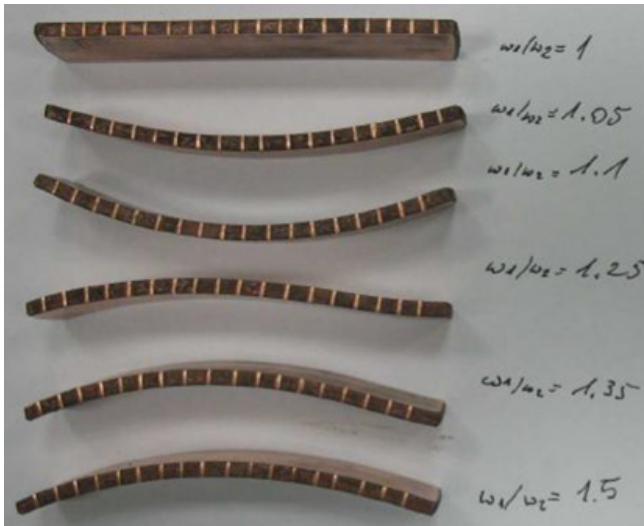


Fig. 9. Shapes of technically pure copper sheets rolled asymmetrically with different ratio of asymmetry (A) [41]

vature has relatively small absolute values starting from $A = 1.3$. These types of changes are caused by characteristic variation of distribution of internal stresses (shown in Fig. 7). The distributions of the shear stress component Σ_{13} are of special importance for this effect. The calculations were done under assumption that there is no loose of contact between the rolls and the material. Our FEM calculations showed that the sample curvature depends on the value of friction parameter (μ) and the best prediction of bending was obtained for the values of μ between 0.3 and 0.4. Therefore one can conclude that the sample curvature can be reduced by an appropriate choice of the rolling anisotropy A .

It should be underlined that minimizing the bending effect is important issue in the asymmetric rolling process. As mentioned above, the possibility of obtaining a nearly straight rolled strip is predicted by FEM calculation for $A \cong 1.2$. This effect was also experimentally verified, e.g., in the case of asymmetrically rolled polycrystalline copper [40]. An explanation of this effect may be as follows. For small differences between rollers velocities and for thicker samples, the layers within the rolled strip are

pleated and as a result the boundary layers of the strip elongate with a similar speed. This can explain why one obtains a nearly flat rolled strip.

Another important parameter in the forming processes is the deformation work W supplied during the rolling. It is presented in Fig. 8c as the ratio W_{AR}/W_{SR} . This ratio strongly increases with the degree of rolling asymmetry A .

6. Texture variation

The $\{200\}$, $\{111\}$ and $\{220\}$ pole figures were determined using X-ray diffraction in three layers of the rolled samples, namely in the top, bottom and central sections. Corresponding ODFs were calculated (cf., [35,36]). All examined textures are presented in $\varphi_2 = 0^\circ$ section of the Euler space (according to Bunge's convention [35]). This section was selected because it contains the Brass (B) component, which is convenient for the analysis of texture modification. Texture of the initial material is shown in Fig. 3 and two ideal orientations are marked in $\varphi_2 = 0^\circ$ section: Brass (B) and Cubic (W) ones. This material was next rolled symmetrically ($A = 1$) and asymmetrically ($A = 1.1$ and $A = 1.5$). Rolling textures predicted by FEM+LW model for three sample layers are compared with the experimental textures of 6061 aluminum in Figs. 10-12. In the predicted SR texture (Fig. 10a) we observe subtle shifts of texture maxima. Let us consider B orientation: in the top material layer the first two maxima of B component are shifted up and the two next ones are shifted down with respect to the horizontal line drawn at $\Phi = 45^\circ$, while the opposite sequence of shifts is observed in the bottom layer. These shifts do not occur in the central layer of SR material: all equivalent B component maxima lie on the horizontal red line (Fig. 10a – centre). The observed effect can be explained by the distribution of the Σ_{13} shear stress component – Fig. 7a – left column. In the top surface layer we observe its variation from positive to negative values and the opposite sequence appears in the bottom surface, while this stress component do not practically appear in the central layer. Corresponding

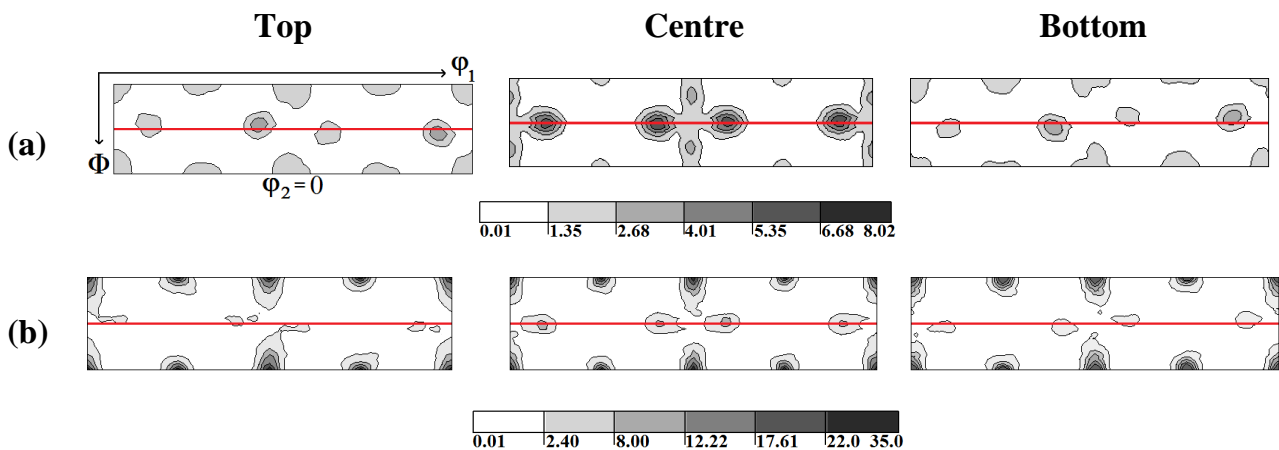


Fig. 10. Textures of symmetrically rolled aluminum ($A = \omega_1/\omega_2 = 1.0$) in top, central and bottom material layers: a) predicted by FEM+LW model, b) determined by X-ray diffraction. $\varphi_2 = 0^\circ$ sections are shown and red line is located at $\Phi = 45^\circ$

shifts of B components appear also in the experimental texture, though this component has lower intensity and its amplitude of shift is smaller – Fig. 10b.

Different behavior is observed in the predicted textures for AR samples. In the case of $A = 1.1$ (Fig. 11a) the shifts of B maxima have the same sign for all three examined material layers: the first two maxima are shifted up and the two next - are shifted down. This effect is clearly visible in the top and central material layers and is weaker in the bottom layer. Similar shifts appear in experimental textures for $A = 1.1$ – Fig. 11b.

Finally, for $A = 1.5$ (Fig. 12) the above-mentioned effect appears still more clearly. In three material layers the shifts of B maxima are the same (the first two are shifted up and the two remaining ones are shifted down). The same behavior was confirmed by experimental textures, though with a slightly smaller amplitude.

Therefore, we conclude that texture is more homogeneous after AR process than after SR one. This behavior can be explained by a nearly homogeneous distribution of the Σ_{13} shear stress component across the sample thickness, as can be seen in Fig. 7c – left column.

The shifts of B texture component, discussed above, can be explained by the rotation of texture around TD. The amplitude of this rotation was analyzed, using FEM calculations, in function of the distance of a material layer from the top surface. The rolled sample was divided into eight layers of the same thickness (which corresponds to the used elements in FEM calculations). In each of the considered layers, the angle Ω was evaluated characterizing the texture rotation around TD. This angle was determined by finding an opposite rotation ($-\Omega$), which restored back the orthorhombic symmetry of texture, i.e. it made it similar to the texture from the central layer of SR material. The variation of such determined angle Ω versus distance from the top surface is shown in Fig. 13a. It can be noted that in the case of SR ($A = 1.0$) the angle Ω changes the sign, when passing from the top to the bottom surface and $\Omega = 0$ appears in the sample center. For $A = 1.05$ the angle Ω changes the sign, but this occurs already closer to the bottom surface. For higher values of A the angle Ω has negative sign everywhere across the sample. Let us note that for $A = 1.5$ and $A = 2.0$ the distribution of Ω versus depth becomes nearly uniform (i.e. curves are nearly flat). Hence we conclude, that texture rotation across the sample is

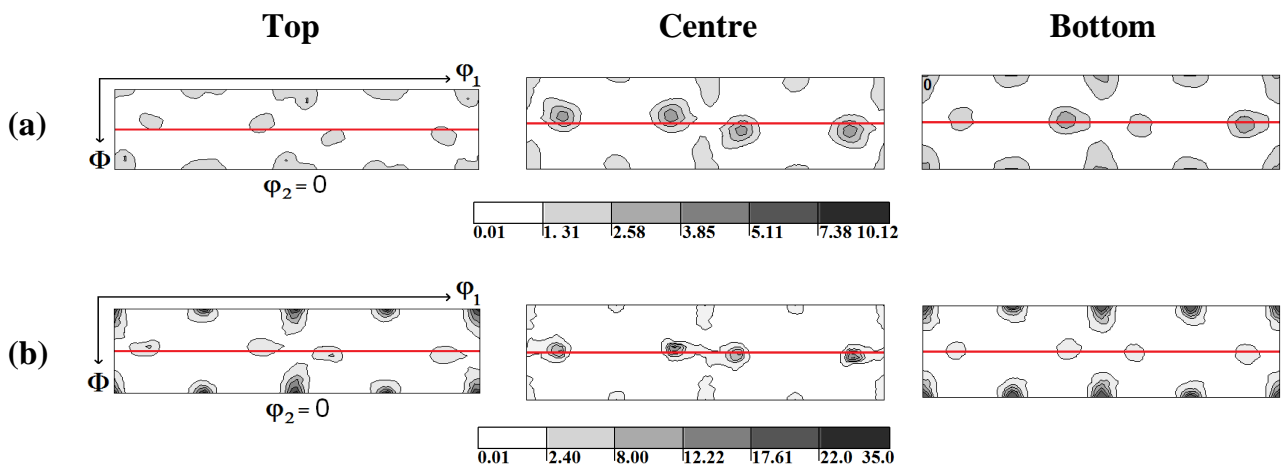


Fig. 11. Textures of asymmetrically rolled aluminum ($A = \omega_1/\omega_2 = 1.1$) in top, central and bottom material layers: a) predicted by FEM+LW model, b) determined by X-ray diffraction. $\varphi_2 = 0^\circ$ sections are shown and red line is located at $\Phi = 45^\circ$

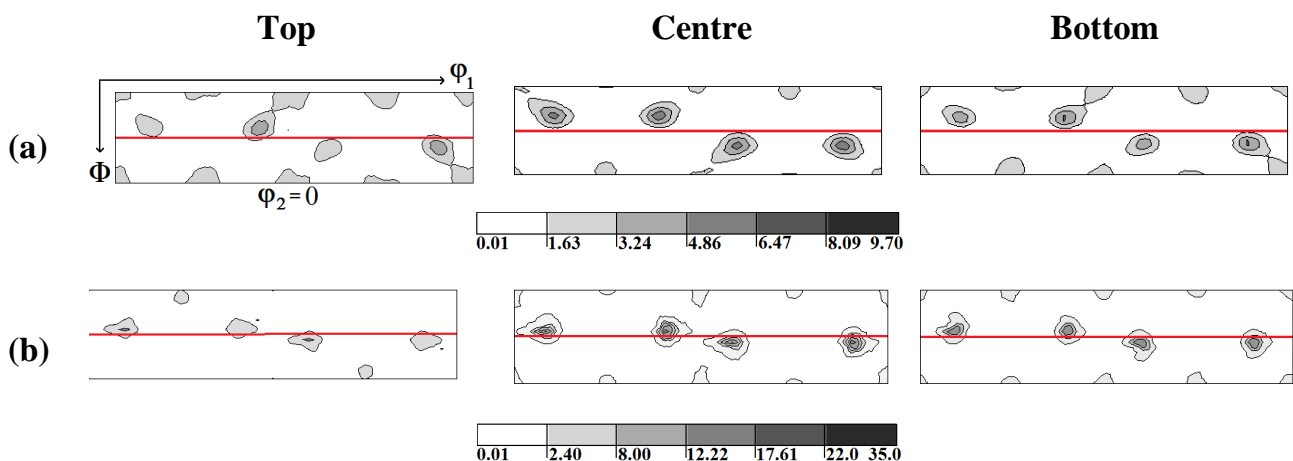


Fig. 12. Textures of asymmetrically rolled aluminum ($A = \omega_1/\omega_2 = 1.5$) in top, central and bottom material layers: a) predicted by FEM+LW model, b) determined by X-ray diffraction. $\varphi_2 = 0^\circ$ sections are shown and red line is located at $\Phi = 45^\circ$

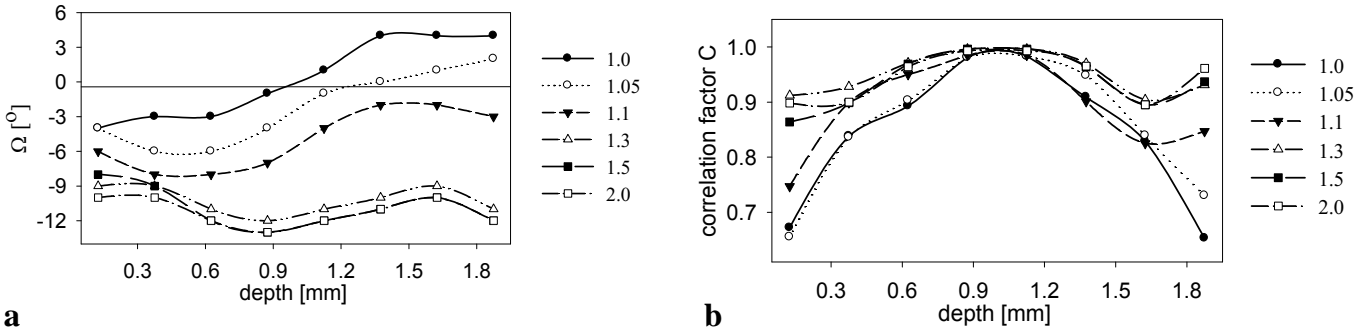


Fig. 13. a) Rotation angle Ω vs. depth for textures from different layers of aluminum sample with reference to the texture of the center layer of symmetrically rolled material, b) correlation factor C expressing similarity of textures from different layers of aluminum sample with respect to the texture of the central layer. The following degrees of rolling asymmetry $A = \omega_1/\omega_2$ were considered: 1.0, 1.05, 1.1, 1.3, 1.5, and 2.0.

much more homogeneously distributed in the AR samples than in the SR one.

Another illustration of texture variation across the sample is shown in Fig. 13b. The rolled material studied by FEM+LW model was divided again into eight layers. The average texture of two central layers served as the reference one. Next, the correlation factor C was determined, according to the procedure developed in [42], to express the similarity between a given texture and the reference one. $C = 1$ means that two textures are identical, and $C = 0$ mean that textures are totally different. The calculated correlation factor C versus depth for different degrees of rolling asymmetry is shown in Fig. 13b. We note that the strongest variation of C appears for low A (equal to 1.0, 1.05 and 1.1). For higher degrees of asymmetry ($A = 1.5$ and $A = 2.0$) the variation of C becomes nearly flat. This confirms again the effect of texture homogenization across the sample thickness after AR.

7. Plastic anisotropy

Texture variation caused by AR modifies physical properties. The example of practical importance is the material plastic anisotropy [43,44]. It can be characterized by Lankford coefficient R , defining the width-to-thickness strains ratio during a tensile test:

$$R = \frac{\varepsilon_W^{pl}}{\varepsilon_T^{pl}} \quad (8)$$

For the rolled textured sheets R coefficient is generally anisotropic. It depends on the orientation of tensile axis with respect to RD, defined by the angle α , hence $R = R(\alpha)$. A practical measure of the plastic anisotropy is given by the average Lankford factor (α is expressed in degs):

$$\langle R \rangle = \frac{1}{4} [R(0) + 2R(45) + R(90)] \quad (9)$$

The variation of $\langle R \rangle$ calculated versus depth for various degrees of rolling asymmetry A is shown in Fig. 14. The values of R were calculated basing on the predicted textures and the procedure developed in [43]. Generally, the values of $\langle R \rangle$ are

higher for AR than after SR processing. The most important differences are observed in the central part of the sample, which represents a major part of material. Let us note that for $A = 1.1$ the distribution of $\langle R \rangle$ is nearly flat. Therefore, we can conclude that AR can be used to modify the plastic anisotropy.

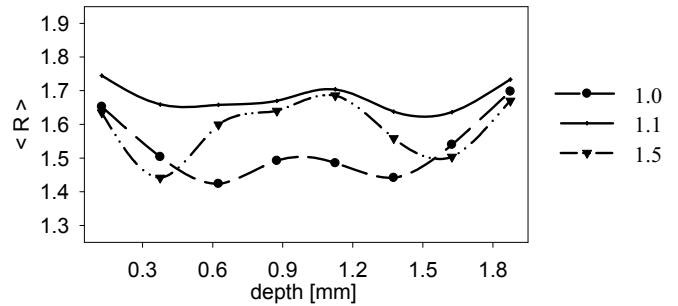


Fig. 14. Calculated average Lankford coefficient $\langle R \rangle$ vs. depth from the top of the sample for different $A = \omega_1/\omega_2$ ratios

8. Conclusions

The obtained theoretical and experimental results lead to the following conclusions:

- strong shear stress component induced during AR causes texture modifications. The obtained textures are rotated around TD comparing with the texture of central layer of SR samples,
- rolling textures are nearly homogeneously distributed across the sample thickness after AR. Also, they are homogeneously rotated around TD,
- normal rolling force in AR is lower than in SR, accordingly to a decrease of Σ_{33} global stress component, which is favorable for rolling mill durability,
- sample curvature occurs after AR. The curvature magnitude can be strongly reduced by an appropriate choice of the rolling asymmetry ratio,
- modification of texture caused by AR influences the material plastic anisotropy. The average Lankford coefficient is generally higher after AR. For some degrees of rolling asymmetry (around $A = 1.1$) the plastic anisotropy is nearly homogeneous across the material thickness.

Acknowledgements

This work was financed by the Polish National Centre for Science (NCN) under decision number: DEC-2013/11/B/ST3/03787.

REFERENCES

- [1] H. Gao, G. Chen, , *Iron and Steel*, **33**, 63-66 (1998).
- [2] S.H. Lee, G.N. Lee, *Int. J. Mech. Sci.* **43**, 1997-2001 (2001).
- [3] J. Sidor, A. Miroux, R. Petrov, L. Kestens, *Acta Mater.* **56**, 2495-2507 (2008).
- [4] J.-S. Lu, O.-K. Harrer, W. Schwenzfeier, F.D. Fischer, *Int. J. Mech. Sci.* **42**, 49-61 (2000).
- [5] H. Kuramae, H. Sakamoto, H. Morimoto, E. Nakamachi, *Procedia Engineering*, **10**, 2250-2255 (2011).
- [6] J. Jiang, Y. Ding, F. Zuo, A. Shan, *Scripta Mater.* **60**, 905-908 (2009).
- [7] Z. Li, L. Fu, B. Fu, A. Shan, *Mat. Sci. Eng. A*, **558**, 309-318 (2012).
- [8] F. Zuo, J. Jiang, A. Shan, J. Fang, X. Zhang, T. Nonferr. *Metal Soc.* **18**, 774-777 (2008).
- [9] J.-Y. Kang, B. Bacroix, H. Reglé, K.H. Oh, H.-C. Lee, *Acta Mater.* **55**, 4935-4946 (2007).
- [10] S. Wroński, K. Wierzbanowski, B. Bacroix, M. Wróbel, E. Rauch, F. Montheillet, M. Wroński, *Arch. Metall. Mater.* **54**, 89-102 (2009).
- [11] F. Zhang, G. Vincent, Y.H. Sha, L. Zuo, J.J. Fundenberger, C. Esling, *Scripta Mater.* **50**, 1011-1015 (2004).
- [12] S. Ucuuncuoglu, A. Ekerim, G.O. Secgin, O. Duygulu, *Journal of Magnesium and Alloys*, **2**, 92-98 (2014).
- [13] X. Huang, K. Suzuki, A. Watazu, I. Shigematsu, N. Saito, *J. Alloy Compd.* **457**, 408-412 (2008).
- [14] M. Wroński, K. Wierzbanowski, M. Wrobel, S. Wronski, B. Bacroix, *Met. Mater. Int.* **21**, 805-814 (2015) .
- [15] F. Simoes, R. Alves de Sousa, J. Gracio, F. Barlat, J. Whan Yoon, *Int. J. Mech. Sci.* **50**, 1372-1380 (2008).
- [16] H. Jin, D.J. Lloyd, *Mat. Sci. Eng. A*, **465**, 267-273 (2007).
- [17] J.-K. Kim, Y.-K. Jee, M.-Y. Huh, *J. Mater. Sci.* **39**, 5365-5369 (2004).
- [18] K.-H. Kim, D. N. Lee, *Acta Mater.* **49**, 2583-2595 (2001).
- [19] E. Nakamachi, H. Kuramae, H. Sakamoto, H. Morimoto, *Int. J. Mech. Sci.* **52**, 146-157 (2010).
- [20] S.K. Kim, J.H. Ryu, K.H. Kim, D.N. Lee, *Mater. Sci. Res. Int.* **8**, 20-25 (2002).
- [21] M. Wronski, K. Wierzbanowski, S. Wronski, B. Bacroix, P. Lipinski, *Int. J. Mech. Sci.* **87**, 258-267 (2014).
- [22] R. Hill, *J. Mech. Phys. Solids*, **13**, 213-222 (1965).
- [23] T. Leffers, *Phys. stat. solidi.* **25**, 337-344 (1968).
- [24] M. Berveiller, A. Zaoui, A., *J. Mech. Phys. Solids.* **26**, 325-344 (1979).
- [25] K. Wierzbanowski, A. Baczmanski, P. Lipinski, A. Lodini, *Arch. Metall. Mater.* **52**, 77-86 (2007).
- [26] K. Wierzbanowski, J. Jura, W.G. Haije, R.B. Helmholtz, *Cryst. Res. Technol.* **27**, 513-522 (1992).
- [27] K. Wierzbanowski, M. Wroński, T. Leffers, *Crit. Rev. Solid State.* **39**, 391-422 (2014).
- [28] K. Wierzbanowski, J. Tarasiuk, B. Bacroix, A. Miroux, O. Castelnau, *Arch. Metall.* **44**, 183-201 (1999).
- [29] S.A.A. Akbari Mousavi , S.M. Ebrahimi, R. Madoliat, *J. Mater. Process. Technol.* **187-188**, 725-729 (2007).
- [30] X. Liu, X. Shi, S. Li, J. Xu G. Wang, *J. Iron Steel Res. Int.* **14**, 22-26 (2007).
- [31] S. Wronski, K. Wierzbanowski, M. Wronski, B. Bacroix, *Arch. Metall. Mater.* **59**, 585-591 (2014).
- [32] H.D. Hibbitt, B.I. Karlson, D. Sorensen, *ABAQUS Example Problems Manual. Rolling of Thick Plates*, pp.485-502, Dassault Systèmes, Paris, 2004
- [33] S. Wronski, B. Ghilianu, T. Chauveau, B. Bacroix, *Mater. Charact.* **62**, 22-34 (2011).
- [34] S. Wronski, B. Bacroix, *Acta Mater.* **76**, 404-412 (2014).
- [35] H.J. Bunge, *Texture Analysis in Material Science*, p. 3-41, 1982 Butterworths, London
- [36] J. Tarasiuk, K. Wierzbanowski, A. Baczmański, *Cryst. Res. Technol.* **33**, 101-118 (1998).
- [37] P.P. Gudur, M.A. Salunkhe, U.S. Dixit, *Int. J. Mech. Sci.* **50**, 315-327 (2008).
- [38] A. Baczmański, K. Wierzbanowski, J. Tarasiuk, M. Ceretti, A. Lodini, *Rev. Metall. – Paris.* **94**, 1467-1474 (1997).
- [39] A. Baczmański, A. Tidu, P. Lipinski, M. Humbert, K. Wierzbanowski, *Mater. Sci. Forum.* **524-525**, 235-240 (2006).
- [40] A. Uniwersał, M. Wróbel, K. Wierzbanowski, S. Wroński, M. Wroński, I. Kalembe-Rec, T. Sak, B. Bacroix, *Mater. Charact.* **118**, 575-583 (2016).
- [41] P. Markowski, MSc Thesis, AGH University of Science and Technology, Kraków, Poland, 2012
- [42] J. Tarasiuk, K. Wierzbanowski, *Phil. Mag. A.* **73**, 1083-1091 (1996).
- [43] M. Arminjon, B. Bacroix, *Acta Mech.* **88**, 219-243 (1991).
- [44] S. Wronski, M. Wrobel, A. Baczmanski, K. Wierzbanowski, *Mater. Charact.* **77**, 116-126 (2013)